Engineering Fracture Mechanics 289 (2023) 109439

Contents lists available at ScienceDirect

Engineering Fracture Mechanics

journal homepage: www.elsevier.com/locate/engfracmech

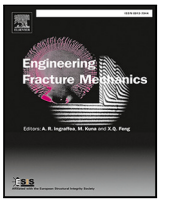

Phase field model for mixed mode fracture in concrete

Ghufranullah khan [a,b], Awais Ahmed [a,c], Yue Liu [d,*], T. Tafsirojjaman [e], Aizaz Ahmad [a], Mudassir Iqbal [a]

[a] University of Engineering and Technology, Peshawar, 25120, Pakistan
[b] Tianjin University, Tianjin, 300072, China
[c] Oslo Metropolitan University, Oslo, 0166, Norway
[d] University of Science and Technology Beijing, 30 Xueyuan Road, 100083, China
[e] The University of Adelaide, South Australia, 5005, Australia

ARTICLE INFO

Keywords:
Phase field model
Cohesive zone model
Mixed mode fracture
Concrete

ABSTRACT

Concrete is a quasi-brittle material and generally fails in mixed mode I-II fracture. The fracture energy release in mode I and mode II during crack propagation is usually different. However, the tensile test fracture toughness has generally been considered in most of the numerical models to study fracture in concrete. In this paper, a phase field model is presented which considers the fracture energy of mode I and mode II for mixed mode I-II fracture simulation in concrete. In addition, it uses a fracture mode controlling parameter χ which, in a sense, controls the governing failure criterion. The post-peak material response is modeled using a cohesive zone approach. The effect of the length scale parameter, mesh size and χ is investigated. For validation, a single-edge notch beam with a notch at various eccentricities is considered. It is shown that the model is mesh independent for a sufficiently fine mesh in cracking region. Also, the effect of the length scale parameter on global response is insignificant. It is observed that $\chi \geq 1$ gives satisfactory results both for mode I and mixed mode I-II fracture in single edge notch concrete beam. The numerical results for the load–displacement curve are compared with the experimental data both qualitatively and quantitatively. It is concluded that the proposed phase field model can simulate mode I and mixed mode I-II fracture in concrete with sufficient accuracy.

1. Introduction

Concrete is widely used in construction industry for building different types of engineering structures. It is quasi-brittle and mostly fails in mixed mode I-II fracture under mechanical and environmental loading [1]. Understanding the crack mechanism and quantifying its damaging effect on concrete structures is indispensable on part of engineers. Once a crack nucleates in concrete under applied load, a tension zone or fracture process zone (FPZ) forms where the material behavior is highly non-linear and involves complicated micro failure mechanisms. This mainly includes an inelastic toughening mechanism, for example micro cracking, crack coalescence, crack deflection, and loss of material integrity [2,3]. The concrete behavior being highly non-linear in FPZ, the classical theory of Linear Elastic Fracture Mechanics (LEFM) cannot be applied to study fracture in concrete. Moreover, the conventional tensile test material fracture toughness is used to predict the damage in concrete, (see for example [4]). In reality, crack propagation is caused by a particular combination of shear and tensile stresses. Consequently, modified crack initiation and damage criterion are

* Corresponding author.
E-mail addresses: ghufranullahkhattak@gmail.com (G. khan), awais.ahmed@uetpeshwar.edu.pk (A. Ahmed), yueliu@ustb.edu.cn (Y. Liu), tafsirojjaman@adelade.edu.au (T. Tafsirojjaman), aizazahmad815@gmail.com (A. Ahmad), mudassiriqbal@uetpeshawar.edu.pk (M. Iqbal).

https://doi.org/10.1016/j.engfracmech.2023.109439
Received 17 December 2022; Received in revised form 2 May 2023; Accepted 15 June 2023
Available online 24 June 2023

required to accurately predict the global structural response. In this paper, a novel phase field model, based on smeared approach, is applied to simulate mode I and mixed mode I-II fracture in concrete.

Numerical modeling of fracture in concrete has been the state-of-the-art research in the last decades. Most of the numerical models tend to avoid singularity encountered in the displacement fields due to cracks. In the technical literature, based on how a crack is represented, two modeling theories are generally used in computational failure mechanics: discontinuous approach or discrete crack model and continuous approach or smear crack model for modeling fracture in solids. In the discrete approach, the crack is represented as an actual physical discontinuity within or between the elements of the finite element mesh. In addition, a softening law is used to define the non-linear behavior of material after peak-load [5,6]. On the other hand, in the smeared approach the material is modeled as a continuum and a modified constitutive relation is used to account for the crack effects. The damage in the material during crack propagation is defined using an internal state variable that acts on the elastic stiffness of the material taking care of the post-peak strain softening as the strain increases [7,8].

The discrete approach is further subdivided into inter-element and intra-element models based on whether the crack is penetrating the elements or going along the boundaries of the elements. The most commonly used inter-element model is the interface element method. It uses zero-thickness elements in regions where there is a probability of crack initiation and propagation. On the other hand, in the extended finite element method (XFEM), the crack propagates across the element of computational mesh and is therefore the most widely used intra-element approach.

In the interface element method, a constitutive relationship based on cohesive interaction [9,10] is used to model the fracture process. Many researchers have used the cohesive approach to investigate fracture in concrete. Graffe and Linero [4] used the interface element method to study fracture in a three-point beam with a notch in the center. A bi-linear softening law was used to model the post-peak behavior of concrete. The numerical results were validated with the experimental results of [11,12]. García-Álvarez et al. [13] used the interface element method in the framework of the cohesive zone model to simulate mixed mode I-II fracture in SEN beam with different notch offsets. A good agreement was observed between the numerical and experimental results for load versus crack mouth displacement (CMD). Gudžulić et al. [14] applied the interface element method to investigate the mechanical response of high-performance plain and fiber-reinforce concrete under cyclic loading. A modified constitutive relation was used to account for the sliding friction and crack opening/closing. Many other researchers have successfully used the cohesive zone-based numerical approaches to study fracture in solids, see for example [15–19]. The interface element is effective when the crack path is known a priori [20]. Additionally, the crack can propagate only along the boundaries of the elements of the computational mesh. Consequently, the mesh orientation and mesh size dictate the crack path [21]. Also, the model is unable to capture the multiaxiality in the FPZ ahead of the crack tip [22]. The adjustment in the stiffness matrix with the crack growth is another challenge to deal with while using this method. These limitations can be overcome using other approaches such as the gradient damage model in [23], a micro polar continuum model in [24] or non-local continuum models in [25].

Another numerical technique that has attracted much attention in recent years is the extended finite element method (XFEM). This method is mesh independent and can easily handle the discontinuities in the displacement field due to crack [26,27]. It does so by using partition of unity (PoU) property proposed in Melenk and Babuška [28] to embed enrichment functions in the classical finite element method at the local level. de Oliveira Pereira et al. [29] used the phantom node method for the parametric study of mixed mode fracture in concrete. Power law [30] based on linear traction-separation law was used to model the damage in the model. Mougaard et al. [31] used XFEM with cohesive zone model to study the mixed mode crack propagation in doubled notched specimen and validated the numerical results with experimental tests of Jacobsen et al. [32]. Many other researchers have used this method to simulate fracture in solids, see for example [33–36]. Although, the PoU-based methods are mesh independent and can handle the strong discontinuities quite well, using them for modeling complex intersecting crack paths, friction and non-linear material behavior are challenging and computationally inefficient.

The smeared crack modeling approach, in contrast to the discrete approach, smears the mechanical effect of the crack in a finite volume and treats the whole body as a continuum with no voids or cracks. These methods can simulate complex crack topologies and are easy to implement in the computational code. Many researchers have used the continuum damage model to simulate crack growth in solids. Gao et al. [37] developed a non-local continuum damage model for brittle fracture and used it to simulate crack growth in single and double-notched concrete beams. Brünig and Michalski [38] developed an anisotropic continuum damage model to study damage in concrete. A modified elastic constitutive relation and damage criterion is proposed to predict the onset and continuation of damage in concrete. Jirásek and Grassl [39] conducted a comparative study using isotropic, anisotropic, and rotating continuum damage models for concrete. Lee and Kim [40] proposed a visco-elastic damage model to study damage in asphalt concrete. The model can successfully predict damage and healing in asphalt concrete under different loading rates and loading modes.

In this work, a smeared approach is used to model fracture in concrete. Specifically, the phase field model proposed by Wang et al. [41] is employed to investigate crack growth in a SEN beam under mode I and mixed mode I-II fracture. The phase field model generalizes Griffith's theory and simultaneously looks for the displacement and crack path by minimizing the total potential energy using a variational approach [42,43]. Bourdin et al. [44] provided the roadmap for the numerical implementation of this approach. In the phase field method, a sharp crack is replaced with a smooth crack having a localized damage band. A length scale parameter is used to control the width of the damage band. A phase field variable is defined which ensures a smooth transition between the intact and damaged state of the material. Compared to Griffith's criterion, which needs a pre-existing crack and cannot capture curvilinear paths, the phase field model does not require any ad-hoc criteria for crack initiation and propagation. The phase field model for crack growth problems has evolved over time. Miehe et al. [45] proposed a thermodynamically consistent phase field model to study brittle fracture in solids. Hou et al. [46] and Ahmed and Khan [47] used the phase field model to simulate fracture

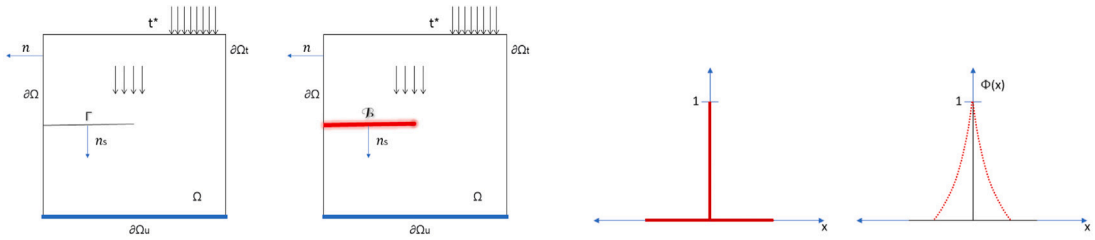

Fig. 1. (a) Discrete crack (left) and phase field crack (right), (b) Discrete crack topology (left) and phase field crack topology (right).

in asphalt concrete at low temperatures. Zhang et al. [48] used a phase field model based on modified G-criterion to simulate mixed mode fracture in rock-like solids. Wu [49] presented a phase field model to study fracture of brittle and cohesive cracks. Wang et al. [41] proposed a unified phase field model to study mixed mode fracture in solids using modified failure criteria.

In this paper a phase field model is presented for the simulation of mode-I and mixed mode I-II fracture in concrete. The phase field model of [41] is used and a unified tensile failure criterion [50] is utilized to predict crack initiation. A modified G-criterion is used for the simulation of mixed mode fracture. To show the performance of the model, mode I and mixed mode I-II fracture is simulated in single edge notch beam with different notch offsets.There are several novel features of the present contribution. Typically, the maximum principal stress criterion is used for predicting crack initiation and propagation in most of the existing phase field models. Whereas, in the present contribution a unified failure criterion [50] is employed, which uses a combination of tensile and shear stress to predict crack growth in concrete. In addition to this, conventionally, fracture energy obtained from tensile tests is utilized for predicting failure in SEN beams in most of phase field models. In this contribution a modified damage criterion is utilized, which takes into consideration the fracture energy of both mode I and mode II fracture modes.

The paper is organized into sections as follows. In Section 2, the phase field model and its implementation in FEM code are introduced. In Section 3, several experimental tests are reproduced to validate the model along with a parametric study. Finally, the important conclusion and summary of the work is reported in Section 4.

2. Unified phase field model

This section contains the regularized framework of the unified phase field model for mixed mode I-II fracture in quasi-brittle materials. Consider a solid body with domain $\Omega \subset \mathbb{R}^n$ $(n = 1, 2, 3)$ and initial reference configuration as shown in Fig. 1(a). The external boundary is represented as a union of $\partial\Omega_t$ and $\partial\Omega_u$ such that $\partial\Omega_t \cup \partial\Omega_u = \partial\Omega$. Also $\partial\Omega_t \cap \partial\Omega_u = \emptyset$. The $\partial\Omega_t$ and $\partial\Omega_u$ are the boundaries corresponding to the applied tractions $\mathbf{t}^*$ and displacements $\mathbf{u}^*$. The body contains a sharp crack represented by Γ. In the phase field model [49], the sharp crack Γ is regularized over a localization band $\mathcal{B}$ (Fig. 1(b)). A diffuse continuous phase field variable $\phi(x) \in [0\ 1]$ is used to predict damage in the localization band as shown in Fig. 1(b). A material is completely damaged when the phase field, $\phi(x) = 1$ and is completely undamaged when $\phi(x) = 0$.

2.1. Smoothing the sharp crack

To make the dissipation energy functional continuous, the sharp crack surface A_s is regularized by replacing it with a diffused functional A_d, leading to

$$A_s = \int_\Gamma d\Gamma = \int_\mathcal{B} \gamma(\phi, \nabla\phi)\, dV = A_d(\phi) \tag{1}$$

in which $\gamma(\phi, \nabla\phi)$ is the crack surface energy density function, a term proposed in [45], which characterizes the crack growth in the spatial domain in terms of phase field variable $\phi(x)$ and its gradient $\nabla\phi(x)$. The generic form of the crack surface density function is defined by [45]

$$\gamma(\phi; \nabla\phi) = \frac{1}{c_o}\left[\frac{1}{l_0}\alpha(\phi) + l_0(\nabla\phi \cdot \nabla\phi)\right] \tag{2}$$

with

$$c_o = 4\int_0^4 \sqrt{\alpha(\beta)}\, d\mathcal{B} \tag{3}$$

in which l_o is the length scale parameter that controls the width of the localized damage band near the crack. A sharp crack γ is recovered for $l_o \to 0$ (Fig. 2(a)). Moreover, geometric crack function $\alpha(\phi) \subset [0\ 1]$ is used to regularize the crack topology in the given domain Ω. It is generally approximated by linear [51] or quadratic polynomial [42,52] as a function of phase field ϕ (Fig. 2(b)). A family of such quadratic functions is given by [49]

$$\alpha(\phi) = \xi\phi + (1 - \xi)\phi^2 \tag{4}$$

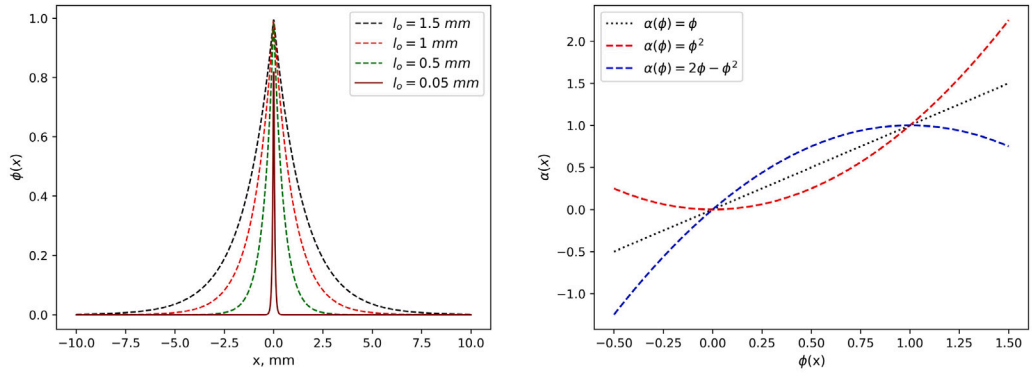

(a) (b)

Fig. 2. Phase field function $\phi(x) = 1 - \exp(|x|/l_o)$ (left) and geometric crack growth functions (right).

2.2. Regularized strain energy functional

According to the first and second law of thermodynamics, the total potential energy Π of a solid body, subject to tractions $\mathbf{t}^*$ and displacements $\mathbf{u}^*$, is always equal to the sum of external potential energy Π^{ext} and internal potential energy Π^{int}. For a crack growth problem, the internal potential energy Π^{int} is constituted by elastic strain energy and dissipation energy, such that

$$\Pi^{int} = E(u, \phi) + D(\phi) \tag{5}$$

in which E is the strain energy and D is the energy dissipated during crack propagation. The regularized strain energy of a body can be written as

$$E(\boldsymbol{\epsilon}(\mathbf{u}, \phi)) = \int_{\Omega} \psi(\phi, \mathbf{u}) dV = \int_{\Omega} g(\phi)\, \psi_o(\mathbf{u}) dV \tag{6}$$

in which $\boldsymbol{\epsilon}(\mathbf{u}, \phi)$ is the small strain tensor, $\psi(\phi, \mathbf{u})$ is the modified strain energy density function and $g(\phi) \in [0\ 1]$ is the degradation/damage function that depends on the phase field $\phi(x)$. The variation of the modified strain energy density functional is defined as

$$\delta E = \int_{\omega} \left(\frac{\partial \psi}{\partial \boldsymbol{\epsilon}} : \nabla^{sym} \delta \mathbf{u} + \frac{\partial \psi}{\partial \phi} \delta \psi \right) \tag{7}$$

2.3. Dissipation energy functional

The dissipation energy functional is used to account for the energy released during crack propagation. It is given as

$$D(\phi) = \int_{B} G_c\ \gamma(\phi, \nabla(\phi))\ dV \tag{8}$$

in which G_c is the fracture energy. The variation of the dissipation function is then defined as

$$\delta D = \int_{B} G_c \delta\gamma\ dV \tag{9}$$

with $\delta\gamma$ being the variation of crack potential, given by

$$\delta\gamma = \frac{1}{c_o} \left[\frac{1}{l_o} \alpha(\phi)' \delta\phi + 2 l_0 \nabla\phi . \nabla \delta\phi \right] \tag{10}$$

The external potential energy Π^{ext} of the body is given by

$$\Pi^{ext} = \int_{\Omega} \mathbf{b}.\mathbf{u} dV + \int_{\partial\Omega_t} \mathbf{t}^*.\mathbf{u} dA \tag{11}$$

in which $\mathbf{b}$ is the body force and $\mathbf{t}^*$ is the traction applied on the body. The variation of Π^{ext} is given by

$$\delta\Pi^{ext} = \int_{\Omega} \mathbf{b}\delta\mathbf{u} dV + \int_{\partial\Omega_t} \mathbf{t}^*\delta\mathbf{u} dA \tag{12}$$

2.4. Constitutive relation

Eq. (7) is supplemented with the two constitutive relations: (i) stress–strain relation, and (ii) energetic crack driving force. The stress–strain relation is defined as

$$\boldsymbol{\sigma} := \frac{\partial \psi}{\partial \boldsymbol{\epsilon}} = g(\phi)\frac{\partial \psi_o}{\partial \boldsymbol{\epsilon}} \tag{13}$$

For a linearly elastic and isotropic material, the elastic strain energy ψ_o is given by

$$\psi_o = \frac{1}{2}\boldsymbol{\epsilon} : \mathbb{E} : \boldsymbol{\epsilon} = \frac{1}{2}\bar{\boldsymbol{\sigma}} : \mathbb{C}_o : \bar{\boldsymbol{\sigma}} \quad \text{with } \bar{\boldsymbol{\sigma}} = \mathbb{E} : \boldsymbol{\epsilon} \tag{14}$$

in which $\mathbb{E}$ and $\mathbb{C}$ are the elastic stiffness and compliance of the material, and $\bar{\boldsymbol{\sigma}}$ is the effective stress tensor. Substituting Eq. (14) in Eq. (13), the constitutive relation becomes

$$\boldsymbol{\sigma} = g(\phi)\bar{\boldsymbol{\sigma}} = g(\phi)\mathbb{E} : \boldsymbol{\epsilon} \tag{15}$$

The non-thermodynamic force Y which drives the evolution of phase field $\phi(x)$ is defined as

$$Y = -\frac{\partial \psi}{\partial \phi} = -g'(\phi)\psi_o = -g'(\phi)\frac{\partial \psi}{\partial g} = -g'(\phi)\overline{Y} \tag{16}$$

in which $\overline{Y} = \frac{\partial \psi}{\partial g}$ is the effective crack driving force related to the strain tensor $\boldsymbol{\epsilon}$. In order to achieve the convergence of non-thermodynamics force Y to a finite value as $\phi \to 1$, it is necessary to satisfy the condition $g(\phi)' = 0$.

2.5. Weak form

Using the variation of internal energy (Eq. (7)), dissipation energy (Eq. (9)), and external energy (Eq. (12)), the variation of the total potential energy can be written as

$$\delta \Pi = \int_\Omega \left(\frac{\partial \psi}{\partial \boldsymbol{\epsilon}} : \nabla^{sym}\delta\mathbf{u} + \frac{\partial \psi}{\partial \phi}\delta\phi \right) dV + \int_B G_c \delta\gamma \; dV + \int_\Omega \mathbf{b}\delta\mathbf{u} dV + \int_{\partial\Omega_t} \mathbf{t}^*\delta\mathbf{u} dA \tag{17}$$

Substituting the constitutive relations defined in Section 2.4, Eq. (17) can be rewritten as

$$\delta \Pi = \int_\Omega (\boldsymbol{\sigma} : \nabla^{sym}\delta\mathbf{u} - Y\delta\phi)\, dV + \int_B G_c \delta\gamma \; dV + \int_\Omega \mathbf{b}\delta\mathbf{u} dV + \int_{\partial\Omega_t} \mathbf{t}^*\delta\mathbf{u} dA \tag{18}$$

which is further simplified into

$$\delta \Pi = \int_\Omega (\boldsymbol{\sigma} : \nabla^{sym}\delta\mathbf{u})\, dV + \int_B (-Y\delta\phi + G_c\delta\gamma) \; dV + \int_\Omega \mathbf{b}\delta\mathbf{u} dV + \int_{\partial\Omega_t} \mathbf{t}^*\delta\mathbf{u} dA \tag{19}$$

Next, the multi-variable problem is written as a system of two homogeneous coupled variational statements by finding the variations $\delta\phi$ and $\delta\mathbf{u}$ as following

$$-\int_\Omega (\boldsymbol{\sigma} : \nabla^{sym}\delta\mathbf{u})\, dV + \int_\Omega \mathbf{b}\delta\mathbf{u} dV + \int_{\partial\Omega_t} \mathbf{t}^*\delta\mathbf{u} dA = 0 \tag{20}$$

$$\int_B (-Y\delta\phi + G_c\delta\gamma) \; dV \leq 0 \tag{21}$$

2.6. Strong form

Using integration by parts and then divergence theorem, Eqs. (20) and (21) become

$$-\int_\Omega (\nabla \cdot \boldsymbol{\sigma} + \mathbf{b})\delta\mathbf{u} \; dV + \int_{\partial\Omega_t} (\mathbf{t}^* - \boldsymbol{\sigma}\cdot\mathbf{n})\delta\mathbf{u} \; dA = 0 \tag{22}$$

$$\int_B (-Y + G_f\partial_\phi\gamma) \; dV + \frac{2l_o}{c_o}G_c \int_{\partial B} (\nabla\phi \cdot \mathbf{n}_s) \leq 0 \tag{23}$$

By applying the stationary condition i.e., $\delta\Pi = 0$ for $\delta\mathbf{u} = 0$ and $\delta\phi > 0$, and $\delta\Pi > 0$ for $\delta\phi = 0$, the following strong form of governing equations is obtained

$$\nabla \cdot \boldsymbol{\sigma} + \mathbf{b} = 0 \quad \text{in} \quad \Omega \tag{24}$$

and

$$\begin{cases} Y - G_c\partial_\phi\gamma = 0 & \dot{\phi} > 0 \\ Y - G_c\partial_\phi\gamma < 0 & \dot{\phi} = 0 \end{cases} \tag{25}$$

with the following Neumann-type boundary conditions

$$\begin{cases} \boldsymbol{\sigma} \cdot \mathbf{n} = \mathbf{t}^* & \text{on } \partial\Omega_t \\ \nabla\phi \cdot \mathbf{n}_s = 0 & \text{on } \partial\mathcal{B} \end{cases} \tag{26}$$

where n_s is the outward normal to the boundary $\partial\mathcal{B}$. These boundary conditions are obtained naturally from the weak form and therefore their explicit imposition is not required in numerical implementation. Eqs. (25) and (26) is commonly called equilibrium and phase field evolution equation.

2.7. Mixed mode I-II evolution equation

In this section, the mixed mode phase field evolution equation is presented. Using Eqs. (10) and (16), Eq. (25) can be rewritten as

$$g(\phi)\frac{\psi_o}{G_c} \geq \frac{2l_o}{c_o}\nabla^2\phi - \frac{\alpha'(\phi)}{c_o l_0} \tag{27}$$

The classical phase field evolution equation (Eq. (27)) [49,53] uses mode I fracture energy. Consequently, these models do not take into account the mode mixity. In addition, the fracture angle is mostly between $\pi/4$ and $\pi/2$ in most of the engineering materials which cannot be obtained using traditional G-criterion [41]. To account for the mode mixity, modified phase field models [48,54] are used with a modified G-criterion [55]. In Wang's model, the following mixed-mode phase field evolution equation is used

$$g_I'(\phi)\frac{\psi_{oI}^+}{G_{cI}} + g_{II}'(\phi)\frac{\psi_{oII}^+}{G_{cII}} \geq \frac{2l_0^2\nabla^2\phi - \alpha'(\phi)}{c_o l_o} \tag{28}$$

where $g_I'(\phi)$ and $g_{II}'(\phi)$ are the degradation functions and G_{Ic} and G_{IIc} are the critical fracture energies of mode I and mode II, retrospectively. The strain energies ψ_{oI}^+ and ψ_{oII}^+ are defined as [41]

$$\psi_{oI}^+ = \begin{cases} \frac{(\sigma^{nn})^2}{2E}, & if \quad \sigma^{nn} > 0 \\ 0, & if \quad \sigma^{nn} < 0 \end{cases} \tag{29}$$

$$\psi_{oII}^+ = \begin{cases} \frac{(\sigma^{nm})^2}{2\mu}, & if \quad \sigma^{nn} > 0 \\ 0, & if \quad \sigma^{nn} < 0 \end{cases} \tag{30}$$

where n and m indicate directions perpendicular and parallel to the crack surface, and σ^{nn} and $\sigma^{nm}(\tau)$ are the normal and shear component of effective stress tensor $\bar{\sigma}$. In Eqs. (29) and (30) it is assumed that σ^{nn} is the first major principal stress.

2.8. Unified tension failure criterion

A unified failure criterion [50] is used to predict the crack initiation under mode I and mixed mode I-II fracture

$$\frac{\sigma^2}{\sigma_t^2} + \frac{\tau^2}{\tau_s^2} = 1 \tag{31}$$

where σ and τ are the tensile and shear stress at the given point and σ_t and τ_s are the critical tensile and critical shear strength fracture plane. Based on the particular value of $\chi = \frac{\tau_s}{\sigma_t}$, Eq. (31) gives different failure criteria (see [41] for more detail).

2.9. Characteristic functions for the cohesive crack

The unified phase field model is supplemented with two characteristic functions: (i) geometric crack growth function $\alpha(\phi)$ and (ii) energetic degradation function $g(\phi)$. These functions are postulated as follows

$$\alpha(\phi) = 2\phi - \phi^2 \tag{32}$$

$$g(\phi) = \frac{(1-\phi)^p}{(1-\phi)^p + P(\phi)} = \frac{1}{1+q(\phi)}, \qquad q(s) = \frac{P(\phi)}{(1-\phi)^p} \tag{33}$$

with

$$P(\phi) = 1 + a_2\phi + a_3\phi^2$$

Where the exponent $p \geq 2$ and $a_1 > 0$. The parameters p, a_1, a_2 and a_3 are determined in terms of tensile strength f_t, critical crack opening w_c, and initial slope k_o of the particular softening law. These parameter are calculated by [49]

$$a_1 = \frac{4l_{ch}}{\pi l_0}, \qquad a_2 = 2(-2k_0\frac{G_c}{f_t^2})^2 - (p+0.5) \tag{34}$$

$$a_3 = \begin{cases} 0, & \text{if } p > 2 \\ \frac{1}{a_2}[\frac{1}{8}(\frac{w_c f_t}{G_c})^2 - (1+a_2)] & \text{if } p = 2 \end{cases} \tag{35}$$

where l_{ch} is the internal length scale that controls the length of FPZ ahead of the crack tip. To get a convex free energy functional, it is mandatory that the length scale parameter $l_o \leq \frac{8l_{ch}}{3\pi}$ [56]. Mostly linear, bilinear or exponential softening laws are used to model fracture in quasi-brittle materials. In this work, a linear softening law [49] is used with the following parameters:

$$p = 2.0, \quad a_1 = \frac{4l_{ch}}{\pi l_o}, \quad a_2 = -0.5, \quad a_3 = 0.0 \tag{36}$$

2.10. Crack irreversibility

To ensure the crack irreversibility, the condition $\dot{\phi} > 0$ needs to be satisfied in the numerical implementation. In this regard, history variables h_I and h_{II} are introduced at step i and $i-1$ and the following algorithm is used to ensure the crack irreversibility [41].

$$\begin{cases} h_I(i) = \frac{\psi^+_{oI}(i)}{\overline{G}_{cI}}, h_{II}(i) = \frac{\psi^+_{oII}(i)}{\overline{G}_{cII}}, & \text{if } \frac{\psi^+_{oI}(i)}{\overline{G}_{cI}} + \frac{\psi^+_{oII}(i)}{\overline{G}_{cII}} > h_I(i-1) + h_{II}(i-1) \\ h_I(i) = h_I(i-1), h_{II}(i) = h_{II}(i-1), & \text{if } \frac{\psi^+_{oI}(i)}{\overline{G}_{cI}} + \frac{\psi^+_{oII}(i)}{\overline{G}_{cII}} \leq h_I(i-1) + h_{II}(i-1) \end{cases} \tag{37}$$

At initial step 0, $h_I(0)+h_{II}(0) = \max[h_{min}, \frac{\psi^+_{oI}(0)}{\overline{G}_{cI}} + \frac{\psi^+_{oII}(0)}{\overline{G}_{cII}}]$, where $h_{min} = \frac{f_t^2}{2E}$. The modified fracture energies $\overline{G}_{cI}$ and $\overline{G}_{cII}$ are defined as

$$\begin{cases} \overline{G}_{cI} = G_{cI}/b_I = \frac{c_o l_o}{2E}\frac{g'(0)}{\alpha'(0)}\sigma_t \\ \overline{G}_{cII} = G_{cII}/b_{II} = \frac{\chi^2 E}{\mu}\overline{G}_{cI} \end{cases} \tag{38}$$

where b_I and b_{II} are constants that can affect the fracture angle during crack propagation [41]. In this work, b_I and b_{II} are taken equal to 1. Finally, Eq. (28) is written in terms of history fields as following

$$g'_I(\phi)h_I + g'_{II}(\phi)h_{II} = \frac{2l_0^2\nabla^2\phi - \alpha'(\phi)}{c_o l_o} \tag{39}$$

2.11. Discretized form

To discretize the governing equations given by Eqs. (20) and (39) using FEM, the displacement and phase field are approximated as

$$\mathbf{u} = \mathbf{N}_u\,\hat{\mathbf{u}} \tag{40}$$

$$\phi = \mathbf{N}_\phi\,\hat{\boldsymbol{\phi}} \tag{41}$$

in which $\hat{\mathbf{u}}$ and $\hat{\boldsymbol{\phi}}$ are the displacement and phase field values at the nodes, $\mathbf{N}_u$ and $\mathbf{N}_\phi$ are the shape function matrices defined as

$$\mathbf{N}_u = \begin{bmatrix} \boldsymbol{\Phi}^1 & 0 & \boldsymbol{\Phi}^2 & 0 & \cdots & \boldsymbol{\Phi}^i & 0 \\ 0 & \boldsymbol{\Phi}^1 & 0 & \boldsymbol{\Phi}^2 & \cdots & 0 & \boldsymbol{\Phi}^i \end{bmatrix} \tag{42}$$

$$\mathbf{N}_\phi = \begin{bmatrix} \boldsymbol{\Phi}^1 & \boldsymbol{\Phi}^2 & \cdots & \boldsymbol{\Phi}^i \end{bmatrix} \tag{43}$$

$\boldsymbol{\Phi}_i$ represents the standard finite element shape function for the ith node. Next, the gradient operator matrices $\mathbf{B}_u$ and $\mathbf{B}_\phi$ are defined for the displacement and the phase field as follows

$$\mathbf{B}_u = \begin{bmatrix} \boldsymbol{\Phi}^1_{,1} & 0 & \boldsymbol{\Phi}^2_{,1} & 0 & \cdots & \boldsymbol{\Phi}^i_{,1} & 0 \\ 0 & \boldsymbol{\Phi}^2_{,2} & 0 & \boldsymbol{\Phi}^2_{,2} & \cdots & 0 & \boldsymbol{\Phi}^i_{,2} \\ \boldsymbol{\Phi}^1_{,2} & \boldsymbol{\Phi}^1_{,1} & \boldsymbol{\Phi}^2_{,2} & \boldsymbol{\Phi}^2_{,1} & \cdots & \boldsymbol{\Phi}^i_{,2} & \boldsymbol{\Phi}^i_{,1} \end{bmatrix} \tag{44}$$

$$\mathbf{B}_\phi = \begin{bmatrix} \boldsymbol{\Phi}^1_{,1} & \boldsymbol{\Phi}^2_{,1} & \cdots & \boldsymbol{\Phi}^i_{1} \\ \boldsymbol{\Phi}^1_{,2} & \boldsymbol{\Phi}^2_{,2} & \cdots & \boldsymbol{\Phi}^i_{2} \end{bmatrix} \tag{45}$$

Then the discretized form of the governing equations (Eqs. (20) and (39)) is derived as

$$\int_\Omega \mathbf{B}_u^T \boldsymbol{\sigma} d\Omega \hat{u} = \int_{\partial\Omega} \mathbf{N}_u^T \mathbf{t}^* dA + \int_\Omega \mathbf{N}_u{}^T \mathbf{b} dV \tag{46}$$

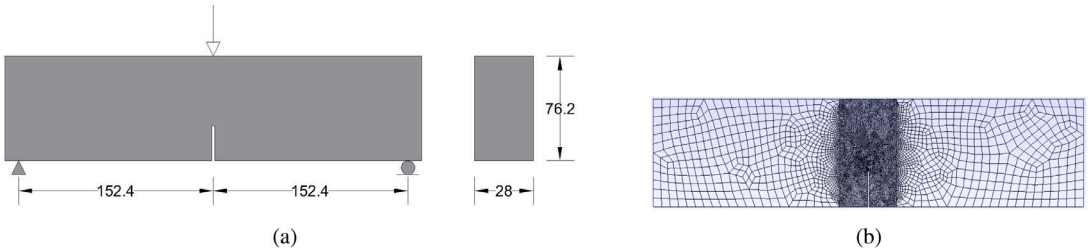

Fig. 3. SEN beam with the notch in the center (left). (b) Discretized geometry of SEN beam.

$$\int_{\Omega} \frac{2l_o}{c_o} \mathbf{B}_{\phi}^{T} \mathbf{B}_{\phi} d\Omega \hat{\phi} + \int_{\Omega} \frac{1}{c_o l_o} \alpha'(\phi) \mathbf{N}_{\phi}^{T} d\Omega + \int_{\Omega} [g_I'(\phi) h_I + g_{II}'(\phi) h_{II}] \mathbf{N}_{\phi}^{T} d\Omega = 0 \tag{47}$$

The loading is increased incrementally and in each loading step Eqs. (46) and (47) is solved. Mostly monolithic [57] or staggered [41,45] schemes are used to solve the governing equations. In this work, a monolithic scheme is employed. However, a diagonal stiffness matrix is used in this work with zero coupling terms and solved through the Newton–Raphson method [58]. Ignoring coupling terms may compromise the convergence rate, but not as severe as in staggered scheme. However, the use of a diagonal stiffness matrix does not affect the accuracy of the model itself and requires a smaller time step to get accurate results [58].

3. Numerical examples

In this section, the modeling ability of the phase field model in simulating diffusive fracture in concrete is demonstrated. Using an open-source JIVE library, the model is programmed in in-built C++ finite element code. The simulations are performed using two-dimensional, linear quadrilateral elements. To ensure adequate resolution of the damage field within the localization band l_o, a sufficiently fine mesh with a mesh size of $s_m = (\frac{1}{5} \sim \frac{1}{10}) l_o$ is used. [49]. In order to obtain converged results for the system of nonlinear equations, a Newton–Raphson iterative scheme is employed. The iterative scheme uses a convergence tolerance of 0.0001. Compression failure is ignored in this contribution. In particular, crack growth under mode I and mixed mode I-II fracture is simulated in a single-edge notched concrete beams. The notch in the beams is considered at various eccentricities. In all the simulations (if not mentioned explicitly), a linear traction-separation law is used and the plane strain conditions are assumed. Additionally, a parametric study related to the length scale parameter, l_o, and the ratio of critical shear strength to critical tensile strength, $\chi = \mu_s/\sigma_t$, is carried out.

3.1. Mode I single edge notch beam

To simulate mode I fracture in concrete, a single-edge notch beam is considered. The geometry of the beam, along with boundary conditions, is shown in Fig. 3(a), with the geometric dimensions given in mm. The beam geometry is discretized using Gmsh software. To obtain accurate results, a relatively fine mesh is used where the crack is likely to propagate i.e the vertical strip shown in Fig. 3(b). The beam geometry is discretized with 7524 linear quadrilateral elements with a mesh size of 0.8 mm in the center of the beam and 6 mm in the remaining region. The boundary conditions of the support, including roller and hinge, are imposed on a singular node in close proximity to the support. Conversely, the boundary condition that corresponds to the applied load is applied on a group of nodes over a span of 1.6 mm. A MATLAB code is used to generate a mesh file, compatible with the in-house built finite element code, that includes nodal coordinates, node connectivity, and nodes corresponding to the applied point load and supports. The elastic material properties are Young's modulus $E = 32.8$ GPa and Poisson's ratio $\nu = 0.21$ [59]. To calibrate the linear traction-separation law, fracture energy $G_c = 100$ J/m^2 and tensile strength $f_t = 2.7$ MPa is considered. It should be noted that the literature [59] lacks definitive values for tensile strength and fracture energy. Therefore, the phase field model is first calibrated for tensile strength and tensile fracture energy for pure mode I fracture test. For the remaining simulations, the same values of these parameters were used. The χ parameter is taken equal to 1.

The simulations are performed with length scale parameter $l_o = 5$ mm which is smaller than the $\frac{8 l_{ch}}{3\pi} = 373$ mm. A displacement-controlled setup is used and displacement u is applied at the top center of the beam. To avoid the dynamic effect of the load, the displacement is applied incrementally with step size $\Delta u = 0.001$ mm in 300 steps with a total displacement of 0.3 mm.

The numerical results for load versus crack mouth opening displacement (CMOD) are compared with experimental results of [59] in Fig. 4(b). The damage pattern is shown in Fig. 4(a). It can be seen that the numerical results agree quite well with the experimental results for mode I fracture in the SEN beam with the notch in the center. It is to note here that the softening behavior of concrete is very complicated. It involves friction at crack interfaces, crack locking and crack kinking. These effects can be included in a model considering microstructural details. Alternately, more advanced softening laws, considering microstructural effects, can be utilized to get more accurate results with the present phase field model. Using a softening curve with a bi-linear type of softening, characterized by a steeper initial descent and a stronger tail, can help to improve the prediction of the softening branch [17]. Fig. 5 shows the damage evolution at different displacements/CMOD. The crack initiates at the notch tip and then propagates along the beam center line. The mechanical behavior is approximately linear up to the peak load, after which the damage zone form and the loading capacity begin to decrease with increasing strain.

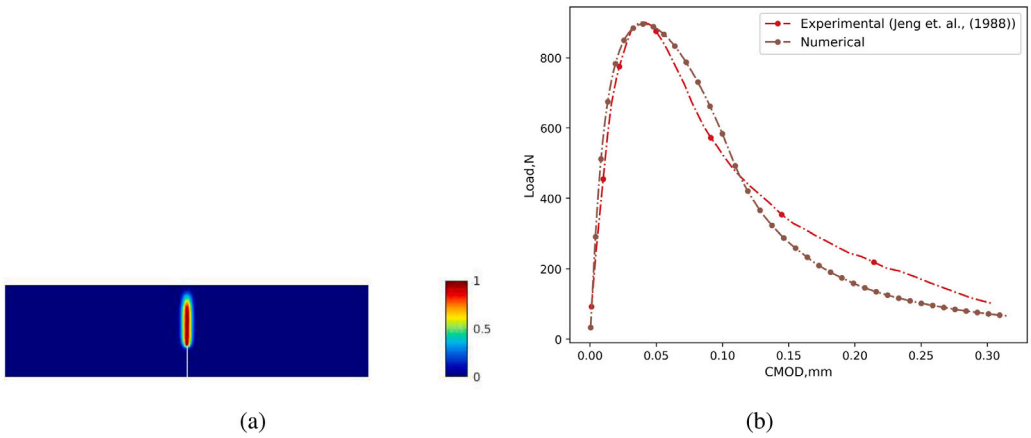

Fig. 4. (a) Damage evolution under mode I and (b) Comparison of the numerical and experimental load–CMOD curve.

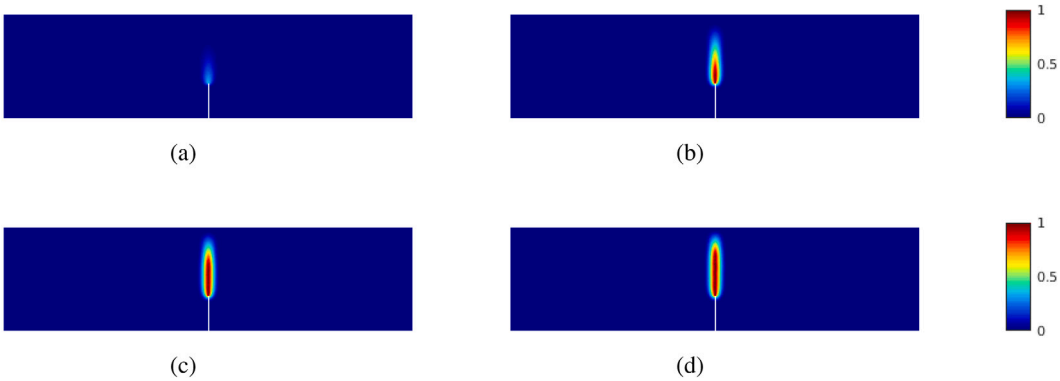

Fig. 5. Damage evolution in single edge notch beam. (a) u = 0.08 mm (CMOD = 0.0642 mm), (b) u = 0.16 mm (CMOD = 0.0642 mm), (c) u = 0.24 mm (CMOD = 0.2434 mm) and (d) u = 0.30 mm (CMOD = 0.3073 mm).

3.2. Effect of mesh size

To study the effect of mesh size on the numerical results, crack growth is simulated in mode I SEN beam with three different mesh sizes: MeshA, MeshB, and MeshC, having a finite element mesh size of 0.6 mm, 0.8 mm and 1 mm in the region with high-stress gradient i.e mostly near the crack. The material properties used in Section 3.1 are considered in the analysis.

The numerical results for load versus CMOD are shown in Fig. 6(b). It is observed that, for the given beam, the numerical results converge for mesh size $s_m \leq 1$ mm. The MeshB is used in the rest of the simulations that follow.

3.3. Effect of length scale parameter

To investigate the effect of length scale parameter l_o on damage zone and numerical results, the SEN beam is analyzed with different length scales, i.e. l_o = 3 mm, 5 mm, 7 mm and 9 mm with a mesh size of 0.8 mm near the crack.

The effect of the length scale on the load–CMOD curve is shown in Fig. 6(a). It is noted that the peak load varies slightly for sufficiently small value for length scale parameter i.e for $l_o < 5$ mm while there is a negligibly small effect on the softening part. This is analogous to the convergence that is obtained by using a sufficiently fine mesh. The length scale parameter is merely regularizing the crack path and controlling the width of the localized damage band (see Fig. 7).

3.4. Mixed mode single edge notch beam

To simulate mixed-mode I-II fracture in concrete, a single-edge notch beam is considered with a notch at various eccentricities. By slightly varying the eccentricity of the notch, the contribution of a shearing fracture mode can be increased or decreased. This allows investigation of the mixed-mode fracture in concrete. For higher notch offsets, there is a significant contribution of mode II, which dictates the fracture angle. Depending on the notch eccentricity, the fracture angles is mostly between $\pi/4$ and $\pi/2$. Consequently, failure occurs under mixed mode I-II. Moreover, the SEN beam with varying notch eccentricity provides some useful

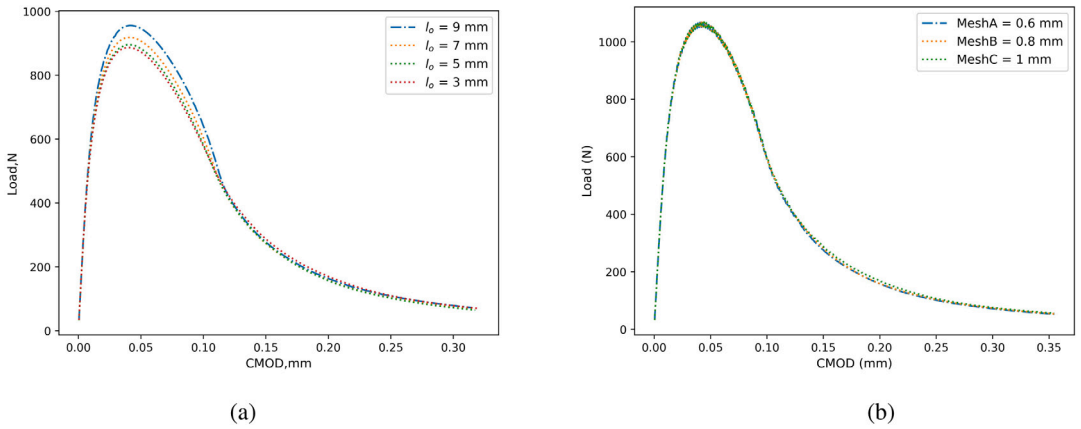

Fig. 6. (a) Effect of length scale parameter on the load–CMOD curve, (b) Effect of mesh size on the load–CMOD curve.

Fig. 7. Damage evolution under different length scales. (a) CMOD = 0.3 mm, l_o = 5 mm, (b) CMOD = 0.3 mm, l_o = 7 mm.

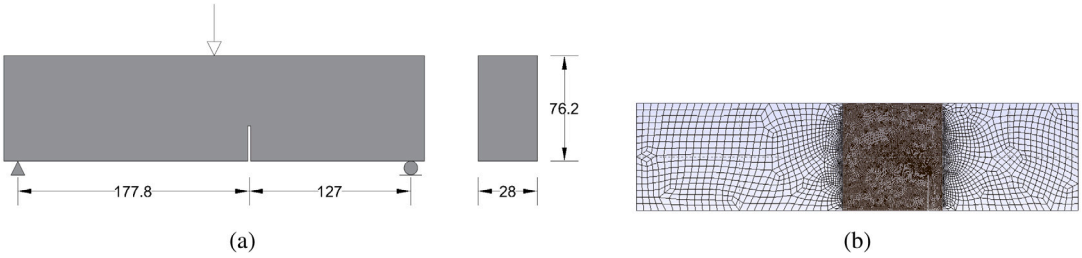

Fig. 8. (a) SEN beam having notch at eccentricity γ = 1/6. (b) Discretized geometry of the SEN beam.

insight into the beam behavior under external loading. First, the strength of the beam varies with the notch eccentricity. Second, the crack does not initiate always at the notch tip; for a notch very close to the support, the crack begins to nucleate from the center. Third, the failure criterion based on $\chi \geq 1$ (Maximum principal stress criterion) mostly governs throughout the beam.

To analyze mixed mode I-II fracture, the mixed mode single edge notch specimen used in [59] is considered. The eccentricity of the notch is increased incrementally by a factor of 1/6 to investigate its mechanical effect on the global response. Fig. 8 shows one such beam having a notch with eccentricity γ = 1/6 along with the discretized geometry. The material properties used in Section 3.1 are considered. They are Young's modulus E = 32.8 GPa, Poisson's ratio ν = 0.21, tensile strength f_t = 2.7 MPa and fracture toughness G_c = 100 J/m^2. A relatively fine mesh with an element size of 0.8 mm is employed near the crack. All simulations are performed using length scale parameter l_o = 5 mm.

The analysis is performed on beams with notch eccentricity γ = 1/6, 2/6, 3/6, and 4/6. The eccentricity γ of the notch is defined as

$$\gamma = \frac{2X}{L} \tag{48}$$

where X is the notch distance from the center line of the beam and L is the span length of the beam. Fig. 9 shows the crack pattern obtained numerically for beams with different notch eccentricities. It is observed that for γ = 1/6, 2/6, and 3/6, the stress gradient is substantial near the notch tip, and thus crack initiates at the crack tip, following the beam center line to the top of the beam. In addition, the crack inclination increases with an increase in notch eccentricity. This is because the model-II contribution increases as the notch eccentricity increases resulting in mixed mode I-II fracture. The numerical investigation indicates that the model can accurately predict changes in failure modes and crack initiation angle in response to change in stresses. The numerically obtained crack patterns appear smooth, but in reality, they are irregular with kinks and branches. This is partly because a smooth crack

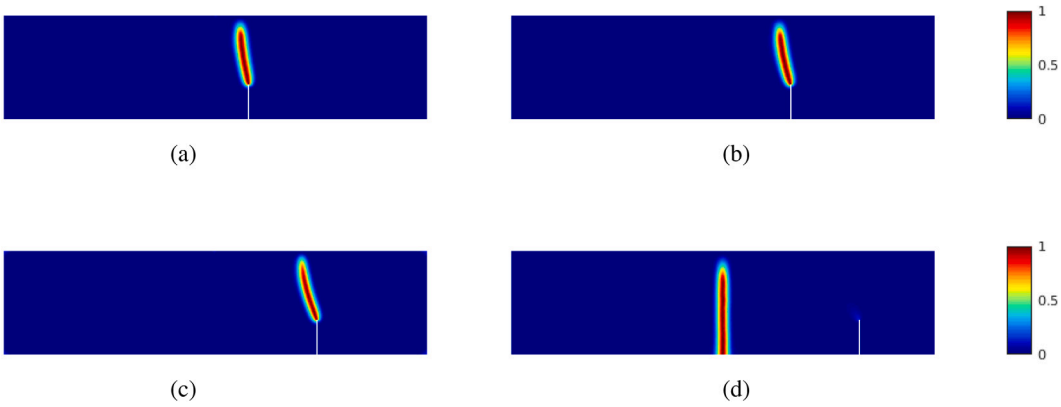

Fig. 9. Damage evolution under mixed mode for beams with eccentric notches. (a) $\gamma = 1/6$, (b) $\gamma = 2/6$, (c) $\gamma = 3/6$ and (d) $\gamma = 4/6$.

potential is used in the model to approximate the crack topology and partly because the concrete medium is assumed homogeneous. In reality, concrete is composed of a hard matrix of cement and coarse and fine aggregate which can have multiple weak irregular fracture planes and thus have kinks and branches in the crack pattern. Fig. 9(d) shows the damage evolution for the notch with eccentricity $\gamma = 4/6$. It can be seen that the crack nucleates from the center of the beam and grows along the beam center line to the top. The crack pattern indicates that failure is purely under mode I with no mode mixity. It is observed that for $\gamma \geq 0.66$, the crack tip is no more the center of the high-stress gradient and fracture flash point. Similar observations are reported for asphalt concrete in [47].

Fig. 10(a) shows the plot of peak load versus eccentricity of the notch. The numerical results are in good agreement with the experimental results of [59]. It can be seen that the peak load increases with an increase in the eccentricity of the notch for $\gamma \leq 0.66$, beyond which variation in strength is insignificant. This indicates that the mechanical effect of the notch is relevant only when it is away from the support.

Fig. 10(b) shows the numerical results for load versus CMOD for the mixed mode beam with different notch offset validate against the experimental results of [59]. It can be observed that the numerical results agree quite well with the experimental results. To improve the prediction of the softening behavior, a bi-linear traction-separation law could be employed [17]. A slight underestimation of the softening response can be attributed to the fact that the numerical model does not consider the effects of friction behavior and cracking locking, which can result in a stronger response in the tail region. It is worth noting that the model can effectively predict the change in softening behavior as the eccentricity is varied.

To investigate how the beam mechanical behavior changes with the eccentricity of the notch, the numerical load versus displacement curve for $\gamma = 0$, 1/6, 2/6, 3/6, 4/6, and 5/6 are compared in Fig. 11(a). It is noted that for a large offset of the notch, the peak load is high but the loss of strength is very rapid. In other words, the concrete behavior is more like a brittle one for higher notch offsets. The load–displacement curves for $\gamma = 4/6$ and 5/6 are nearly identical. This is because for these beams the crack initiates at the center which gives a similar peak load and softening behavior. Fig. 11(b) compares the energy dissipation curve for different eccentricities. It is evident from Fig. 11(b) that the beam stiffness increases only up to the critical eccentricity, beyond which there is no significant increase in the stiffness. Moreover, the energy gradient changes gradually for smaller notch offsets but abruptly once the eccentricity exceeds the critical value i.e $\gamma = 0.66$, indicating a shift from quasi-brittle to brittle fracture. Fig. 11(b) also indicates that the total energy dissipated increases with the increase in notch eccentricity. These observations are consistent with the experimental finding in [59]. Similar observations were reported for asphalt concrete by Ahmed and Khan [47].

3.5. Effect of χ

The χ parameter in Wang's model, in a sense, control the crack initiation criterion and different crack initiation criterion can be recovered based on a range of χ values. To find out its effect on the numerical results and identify the suitable χ value for mode I and mixed mode I-II fracture simulation in concrete, an extensive study is carried out. In this regard, the pure mode I ($\gamma = 0$) and mixed-mode I-II ($\gamma = 1/6$) fracture in single edge notch (SEN) beam is simulated using different χ values i.e. $\chi = 0.01$,0.3,0.5 and 1. The material and geometric properties in Section 3.1 are considered. The computational time increases sufficiently for $\chi < 1$ and the simulation truncates at different stages of the load–CMOD curve (mostly close to the peak load). However, the results can be used to judge the suitable value of χ for analyzing fracture in the SEN beam.

Fig. 12 compares the numerical load–CMOD curve for $\chi = 0.01$, 0.3, 0.5, and 1 with the experimental results. It is observed that the numerical results over estimate the actual member response significantly for $\chi < 1$ both in mode I (Fig. 12(a)) and mixed-mode I-II (Fig. 12(b)). This is because $\chi < 1$ gives a shear-based failure criterion. Consequently, the shear stresses need to exceed the critical shear strength μ_s of concrete for failure to occur. In reality, the damage region is dominated by tensile stresses and has negligible shear stresses. This results in premature truncation and over estimation of member response under loading. The $\chi = 1$

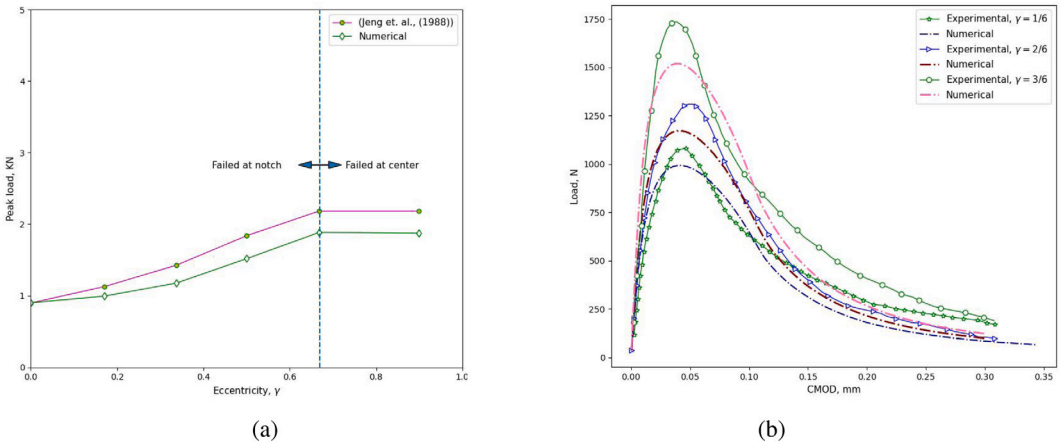

Fig. 10. Comparison of numerical and experimental results. (a) Peaks load-eccentricity and (b) Load–CMOD.

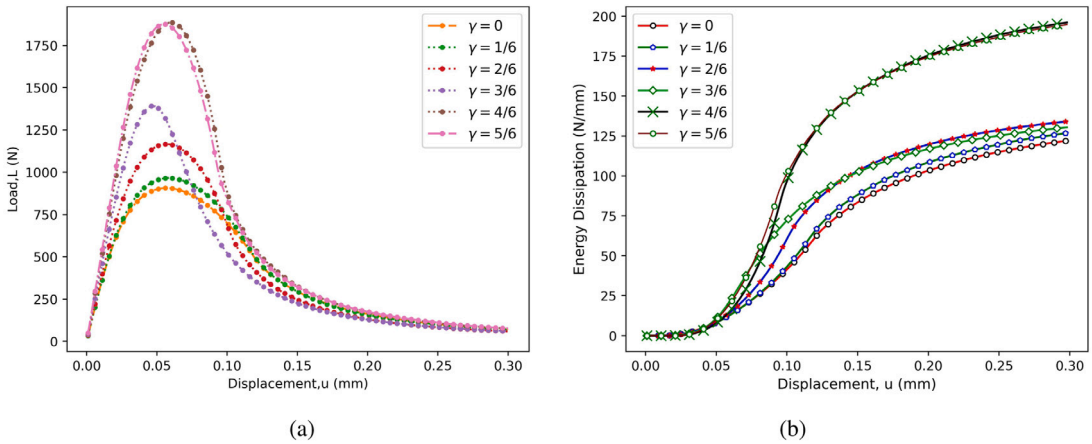

Fig. 11. Load–displacement (left) and energy dissipation curve (right) for different notch eccentricities.

gives more accurate numerical results which can be attributed to the fact that for $\sigma_t = \mu_s$, the maximum principal stress criterion governs which better suits the nature of stresses in the damaged region. It is further observed that within the range $1 \leq \chi \leq 10$, the χ parameter has no effect on numerical results. García-Álvarez et al. [13] noted that the ratio $1 \leq G_{cII}/G_{cI} \leq 100$ can be used for SEN beam with an eccentric notch, which is consistent with our observations. Both statements are equivalent because χ parameter is related to the ratio G_{cII}/G_{cI} by

$$\chi = \sqrt{G_{cII}/G_{cI}} \tag{49}$$

In Fig. 13, the damage patterns obtained using different χ values are shown for mode I ($\gamma = 0$) and mixed mode ($\gamma = 1/6$) beam. When $\chi = 0.01$ for both beams, a well-shaped damage pattern is obtained (Fig. 13(a),13(c)), which is inconsistent with the experimental observations [59]. However, for $\chi \geq 1$, a single crack initiates at the notch tip and propagates to the top of the beam (Fig. 13(b),13(d)). This indicates that for $\chi \geq 1$, both the damage pattern and numerical results are consistent with the experimental observations in [59].

4. Summary and conclusions

A phase field model is used to simulate mode I and mixed mode I-II fracture in concrete. The damage is smeared over a localized band whose width is controlled by the length scale parameter. A phase field variable ϕ is used to indicate the damage in the material. Its values vary between 1 and 0, $\phi = 1$ shows a completely undamaged while $\phi = 1$ shows a completely damaged state of the material. The model is mesh independent, computationally efficient, and does not require a crack-tracking algorithm. This makes it easy to implement it in a finite element code. A linear softening law is used to approximate the nonlinear behavior ahead of the crack tip. The model is implemented in in-house built finite element code using the C++ JEM library.

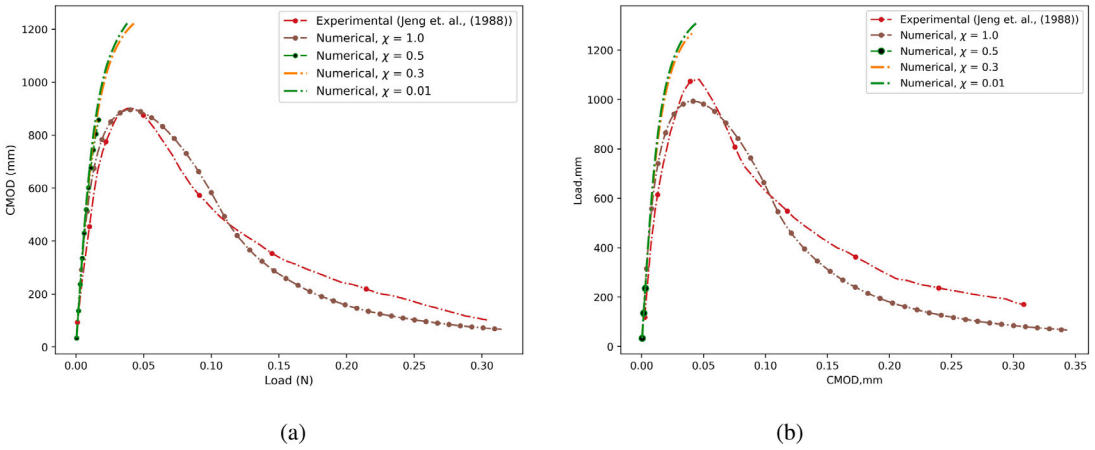

Fig. 12. Load–displacement curve and energy dissipation curve for different notch eccentricities. (a) $\gamma = 0$, and (b) $\gamma = 1/6$.

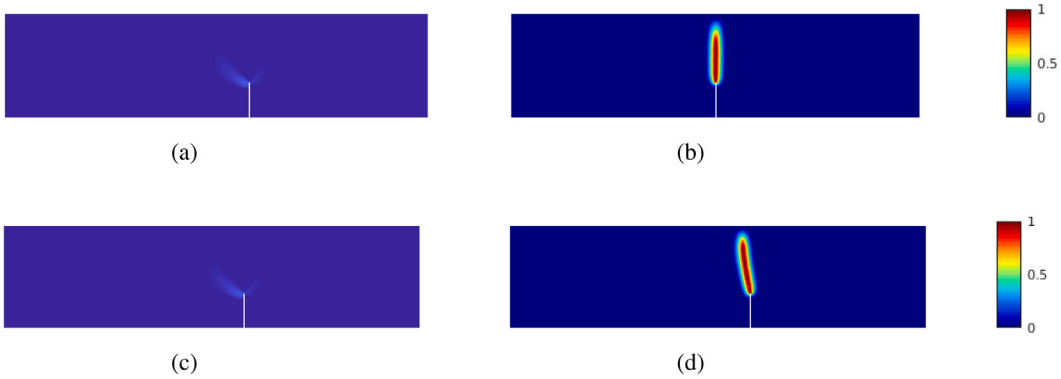

Fig. 13. Damage pattern in mode I and mixed mode beam using different χ values. (a) $\gamma = 0$, $\chi = 0.01$, (b) $\gamma = 0$, $\chi = 1$, (c) $\gamma = 1/6$, $\chi = 0.01$ and (d) $\gamma = 1/6$, $\chi = 1$.

The model is used to investigate fractures in concrete, specifically under mode I and mixed mode I-II in a SEN beam. The numerical results show good agreement with the experimental results both qualitatively and quantitatively. The effect of length scale parameter l_o, mesh size and χ is studied. It is observed that the length scale parameter has very little effect on the global response as long as it mimics the sharp crack. A mesh sensitivity analysis revealed that the model is mesh independent. Moreover, it is concluded that for a single edge notch concrete beam, the critical tensile strength is always equal or smaller than the shear strength i.e. $\chi = \mu_s/\sigma_t \geq 1$. Simulations performed using different notch offset revealed that the beam behavior changes from quasi-brittle to brittle as the notch moves close to the support. Moreover, beyond a certain limit of notch eccentricity, the crack nucleates in the center of the beam and fracture is purely under mode I. The phase field model is utilized to study concrete fracture under quasi-static loading. In future work, the model can be extended to analyze fracture under dynamic and cyclic loading by integrating the effect of rate in the regularized constitutive laws.

CRediT authorship contribution statement

Ghufranullah khan: Software, Methodology, Formal analysis, Conceptualization, Writing. **Awais Ahmed:** Software, Project administration, Methodology, Conceptualization. **Yue Liu:** Resources, Revision, Funding acquisition. **T. Tafsirojjaman:** Funding acquisition, Conceptualization. **Aizaz Ahmad:** Revision, Editing. **Mudassir Iqbal:** Writing – review & editing, Project administration.

Declaration of competing interest

The authors declare that they have no known competing financial interests or personal relationships that could have appeared to influence the work reported in this paper.

Data availability

Data will be made available on request.

References

[1] Wu Z-M, Rena CY, Sun C-Y, Wang Y-J, Zhang X-X, Fei X-D. A new test method for the complete load-displacement curve of concrete under mixed mode I-II fracture. Theor Appl Fract Mech 2020;108:102629.
[2] Frosch RJ. Another look at cracking and crack control in reinforced concrete. Struct J 1999;96(3):437–42.
[3] Shi Z. Crack analysis in structural concrete: theory and applications. Butterworth-Heinemann; 2009.
[4] Graffe R, Linero D. Simulación numérica del proceso de fractura en modo I de vigas de concreto con trayectoria de fisuración conocida mediante un modelo discreto de fisura cohesiva. Revista IngenieríA de Const 2010;25(3):399–418.
[5] Hillerborg A, Modéer M, Petersson P-E. Analysis of crack formation and crack growth in concrete by means of fracture mechanics and finite elements. Cem Concr Res 1976;6(6):773–81.
[6] Gálvez J, Červenka J, Cendón D, Saouma V. A discrete crack approach to normal/shear cracking of concrete. Cem Concr Res 2002;32(10):1567–85.
[7] Rots JG, Nauta P, Kuster G, Blaauwendraad J. Smeared crack approach and fracture localization in concrete. Heron 1985;30(1):1985.
[8] Comi C, Perego U. Fracture energy based bi-dissipative damage model for concrete. Int J Solids Struct 2001;38(36–37):6427–54.
[9] Dugdale DS. Yielding of steel sheets containing slits. J Mech Phys Solids 1960;8(2):100–4.
[10] Barenblatt GI. The mathematical theory of equilibrium cracks in brittle fracture. Adv Appl Mech 1962;7:55–129.
[11] Lotfi HR, Shing PB. Embedded representation of fracture in concrete with mixed finite elements. Internat J Numer Methods Engrg 1995;38(8):1307–25.
[12] Kormeling H, Reinhardt H. Determination of the fracture energy of normal concrete and epoxy-modified concrete. Stevin laboratory 5-83-18. Delft University of Technology; 1982.
[13] García-Álvarez VO, Gettu R, Carol I. Numerical analysis of mixed mode fracture in concrete using interface elements. In: Proceedings of the european congress on computational methods in applied sciences and engineering, barcelona, spain. 2000, p. 11–4.
[14] Gudžulić V, Neu GE, Meschke G. Numerical analysis of plain and fiber reinforced concrete structures during cyclic loading: Influence of frictional sliding and crack roughness. PAMM 2021;20(1):e202000167. http://dx.doi.org/10.1002/pamm.202000167.
[15] Elices M, Guinea G, Gomez J, Planas J. The cohesive zone model: Advantages, limitations and challenges. Eng Fract Mech 2002;69(2):137–63.
[16] Song SH, Paulino GH, Buttlar WG. Simulation of crack propagation in asphalt concrete using an intrinsic cohesive zone model. J Eng Mech 2006;132(11):1215–23.
[17] Sancho J, Planas J, Gálvez J, Reyes E, Cendón D. An embedded cohesive crack model for finite element analysis of mixed mode fracture of concrete. Fatigue Fract Eng Mater Struct 2006;29(12):1056–65.
[18] Wu T, Wriggers P. Multiscale diffusion–thermal–mechanical cohesive zone model for concrete. Comput Mech 2015;55(5):999–1016.
[19] Paulino GH, Song SH, Buttlar WG. Cohesive zone modeling of fracture in asphalt concrete. In: Proceedings of the 5th international RILEM conference–cracking in pavements: mitigation, risk assessment, and preservation. Limoges, France; 2004, p. 63–70.
[20] Wu L, Li Z, Huang S. A comparison of cohesive crack model and crack band model in concrete fracture. In: Applied mechanics and materials, Vol. 170. Trans Tech Publ; 2012, p. 3375–80.
[21] Zhou F, Molinari J-F. Dynamic crack propagation with cohesive elements: A methodology to address mesh dependency. Internat J Numer Methods Engrg 2004;59(1):1–24.
[22] Bažant ZP, Jirásek M. Nonlocal integral formulations of plasticity and damage: Survey of progress. J Eng Mech 2002;128(11):1119–49.
[23] De Borst R, Mühlhaus H-B. Gradient-dependent plasticity: Formulation and algorithmic aspects. Internat J Numer Methods Engrg 1992;35(3):521–39.
[24] Steinmann P, Willam K. Finite-element analysis of elastoplastic discontinuities. J Eng Mech 1994;120(11):2428–42.
[25] Bažant ZP, Oh BH. Crack band theory for fracture of concrete. Matériaux Et Const 1983;16(3):155–77.
[26] Moës N, Dolbow J, Belytschko T. A finite element method for crack growth without remeshing. Internat J Numer Methods Engrg 1999;46(1):131–50.
[27] Dolbow J, Moës N, Belytschko T. An extended finite element method for modeling crack growth with frictional contact. Comput Methods Appl Mech Engrg 2001;190(51–52):6825–46.
[28] Melenk J, Babuška I. The partition of unity finite element method: Basic theory and applications. Comput Methods Appl Mech Engrg 1996;139(1):289–314. http://dx.doi.org/10.1016/S0045-7825(96)01087-0, URL https://www.sciencedirect.com/science/article/pii/S0045782596010870.
[29] de Oliveira Pereira RM, Sanchez ECM, Roehl D. A parametric study of mixed-mode fracture propagation in concrete using Xfem. 2017.
[30] Camanho PP, Dávila CG. Mixed-mode decohesion finite elements for the simulation of delamination in composite materials. Technical report, 2002.
[31] Mougaard JF, Poulsen PN, Nielsen LO. Modelling concrete structures applying XFEM with a mixed mode constitutive model. In: Proceedings of the FraMCo. Jeju, Korea; 2010, p. 23–8.
[32] Jacobsen JS, Poulsen PN, Olesen JF. Measurement and characterization of mixed mode fracture in concrete. In: Fracture mechanics of concrete and concrete structures-recent advances in fracture mechanics of concrete. 2010, p. 717–23.
[33] Lancaster I, Khalid H, Kougioumtzoglou I. Extended FEM modelling of crack propagation using the semi-circular bending test. Constr Build Mater 2013;48:270–7.
[34] Xiaoge T, Zhang R, Yang Z, Chu Y, Zhen S, Xv Y. Simulation of bending fracture process of asphalt mixture semicircular specimen with extended finite element method. Adv Mater Sci Eng 2018;2018.
[35] Mahmoud E, Saadeh S, Hakimelahi H, Harvey J. Extended finite-element modelling of asphalt mixtures fracture properties using the semi-circular bending test. Road Mater Pavement Des 2014;15(1):153–66.
[36] Rashadul Islam M, Vallejo MJ, Tarefder RA. Crack propagation in hot mix asphalt overlay using extended finite-element model. J Mater Civ Eng 2017;29(5):04016296.
[37] Gao Z, Zhang L, Yu W. A nonlocal continuum damage model for brittle fracture. Eng Fract Mech 2018;189:481–500.
[38] Brünig M, Michalski A. A stress-state-dependent continuum damage model for concrete based on irreversible thermodynamics. Int J Plast 2017;90:31–43.
[39] Jirásek M, Grassl P. Evaluation of directional mesh bias in concrete fracture simulations using continuum damage models. Eng Fract Mech 2008;75(8):1921–43.
[40] Lee H-J, Kim YR. Viscoelastic continuum damage model of asphalt concrete with healing. J Eng Mech 1998;124(11):1224–32.
[41] Wang Q, Feng Y, Zhou W, Cheng Y, Ma G. A phase-field model for mixed-mode fracture based on a unified tensile fracture criterion. Comput Methods Appl Mech Engrg 2020;370:113270.
[42] Bourdin B, Francfort GA, Marigo J-J. Numerical experiments in revisited brittle fracture. J Mech Phys Solids 2000;48(4):797–826.
[43] Francfort GA, Marigo J-J. Revisiting brittle fracture as an energy minimization problem. J Mech Phys Solids 1998;46(8):1319–42.
[44] Bourdin B, Francfort GA, Marigo J-J. The variational approach to fracture. J Elasticity 2008;91(1):5–148.
[45] Miehe C, Welschinger F, Hofacker M. Thermodynamically consistent phase-field models of fracture: Variational principles and multi-field FE implementations. Internat J Numer Methods Engrg 2010;83(10):1273–311.
[46] Hou Y, Yue P, Xin Q, Pauli T, Sun W, Wang L. Fracture failure of asphalt binder in mixed mode (modes I and II) by using phase-field model. Road Mater Pavement Des 2014;15(1):167–81.
[47] Ahmed A, Khan R. A phase field model for damage in asphalt concrete. Int J Pavement Eng 2022;23(12):4320–32.
[48] Zhang X, Sloan SW, Vignes C, Sheng D. A modification of the phase-field model for mixed mode crack propagation in rock-like materials. Comput Methods Appl Mech Engrg 2017;322:123–36.

[49] Wu J-Y. A unified phase-field theory for the mechanics of damage and quasi-brittle failure. J Mech Phys Solids 2017;103:72–99.
[50] Zhang Z, Eckert J. Unified tensile fracture criterion. Phys Rev Lett 2005;94(9):094301.
[51] Pham K, Amor H, Marigo J-J, Maurini C. Gradient damage models and their use to approximate brittle fracture. Int J Damage Mech 2011;20(4):618–52.
[52] Alessi R, Marigo J-J, Vidoli S. Gradient damage models coupled with plasticity: Variational formulation and main properties. Mech Mater 2015;80:351–67.
[53] Miehe C, Hofacker M, Welschinger F. A phase field model for rate-independent crack propagation: Robust algorithmic implementation based on operator splits. Comput Methods Appl Mech Engrg 2010;199(45–48):2765–78.
[54] Bryant EC, Sun W. A mixed-mode phase field fracture model in anisotropic rocks with consistent kinematics. Comput Methods Appl Mech Engrg 2018;342:561–84.
[55] Shen B-t, Stephansson O. Modification of the G-criterion for crack propagation subjected to compression. Eng Fract Mech 1994;47(2):177–89.
[56] Wu J-Y. Robust numerical implementation of non-standard phase-field damage models for failure in solids. Comput Methods Appl Mech Engrg 2018;340:767–97.
[57] Liu P, Chen J, Lu G, Wang D, Oeser M, Leischner S. Numerical simulation of crack propagation in flexible asphalt pavements based on cohesive zone model developed from asphalt mixtures. Materials 2019;12(8):1278.
[58] Molnár G, Gravouil A. 2D and 3D abaqus implementation of a robust staggered phase-field solution for modeling brittle fracture. Finite Elem Anal Des 2017;130:27–38.
[59] Jenq Y, Shah S. Mixed-mode fracture of concrete. Int J Fract 1988;38(2):123–42.